Journal of Membrane Science 691 (2024) 122249

Contents lists available at ScienceDirect

Journal of Membrane Science

journal homepage: www.elsevier.com/locate/memsci

Methods to modify supersaturation rate in membrane distillation crystallisation: Control of nucleation and crystal growth kinetics (including scaling)

A. Ouda, Y. Bajón-Fernández, E. McAdam *

Cranfield Water Science Institute, Cranfield University, UK

ARTICLE INFO

Keywords:
Brine management
Resource recovery
Crystal growth
Hollow fibre
Zero-liquid discharge

ABSTRACT

While water vapour flux is often regarded as the critical parameter in membrane distillation crystallisation (MDC), there are multiple factors that will determine the kinetics of nucleation and crystal growth. A Nývlt-like equation is therefore introduced that can relate how multiple conditional parameters (membrane area, flux, temperature difference, crystalliser volume, magma density) independently modify nucleation rate and supersaturation, enabling a normalising approach for the characterisation of nucleation and crystal growth kinetics within MDC. Each parameter can be modified to increase supersaturation rate, which reduced induction time and broadened the metastable zone width (MSZW) at induction. An increase in supersaturation mitigated scaling and favoured bulk nucleation. This is due to the increase in volume free energy provided by the elevated supersaturation that reduces the critical energy requirement for nucleation to favour a homogeneous primary nucleation mechanism. An increase in temperature difference or magma density narrowed the MSZW. For each parameter, either supersaturation rate, supersaturation or induction time were fixed, while the other two factors were amended. While higher supersaturation rates generally favoured larger crystal sizes with broader size distributions, a high level of supersaturation at a low supersaturation rate increased particle size and narrowed the size distribution. In practice, these factors may be applied collectively and synergistically to deliver strict control over crystal growth, which remains a challenge for current evaporative technology. This was illustrated when facilitating an increase in supersaturation rate with membrane area, where an identical nucleation order was identified between membrane systems, from which it can be implied that MDC affords an inherently scalable solution for crystallisation.

1. Introduction

Membrane distillation crystallisation (MDC) is an emerging method for zero liquid discharge that can increase pure water production through the direct treatment of hypersaline brines, while simultaneously instigating creation of a crystalline phase [1,2]. Membrane distillation offers well-defined interfacial area over which mass and heat transfer are controlled to achieve good regulation of the evaporation rate [3,4]. This can provide for the homogeneous regulation of supersaturation, which is critical for controlling the kinetics of nucleation and crystal growth in membrane distillation crystallisation (MDC) [5,6]. Mass and heat transfer mechanisms introduce temperature and concentration polarisation phenomenon within the interfacial boundary layer adjacent to the membrane [7]. It is the difference in supersaturation between the boundary layer and the bulk solution which implies that MDC may be able to decouple primary nucleation, which is thought to occur within the boundary layer, from crystal growth which dominates in the bulk solution [8,9]. The membrane is considered advantageous for crystallisation, as the contact angle can lower the energy barrier to instigate primary heterogeneous nucleation which is beneficial to solutes characterised by low supersaturation and long induction times [10]. However, the occurrence of nucleation at the membrane surface can also induce scaling which has a deleterious effect on membrane performance [11,12].

The rate at which supersaturation is achieved, will determine the extent of supersaturation at the point of nucleation [13]. The extent of supersaturation is also called the metastable limit. The area between the solubility curve and the metastable limit curve is described as the

---

* Corresponding author.
E-mail address: e.mcadam@cranfield.ac.uk (E. McAdam).

https://doi.org/10.1016/j.memsci.2023.122249
Received 28 July 2023; Received in revised form 3 November 2023; Accepted 3 November 2023

metastable zone width (MSZW) [14]. According to Sangwal [15], the MSZW is linearly related to the supersaturation rate. Consequently, a high supersaturation rate will yield a high nucleation rate. At the upper limit of the MSZW, there exists a labile region where supersaturation lowers the free energy barrier sufficiently for spontaneous primary nucleation to proceed. In principle, these conditions do not require a heterogeneous substrate to initiate nucleation (homogeneous nucleation), which could be advantageous to membrane systems as it implies the potential to limit scaling. However, high supersaturation rates can favour smaller crystal sizes with broad size distributions [7,16]. Therefore, there may exist regions within the MSZW that can foster a compromise between the nucleation kinetics which limit scaling, and crystal growth conditions that elicit favourable product characteristics. Close control of the crystal size distribution (CSD) is important as crystal morphology, size and purity can be important for final application, while fines formation should be avoided to simplify downstream separations [8,16].

In MDC, the water vapour flux can be used to modify the supersaturation rate, therefore determining where within the MSZW that nucleation is initiated. The vapour pressure difference is fixed using the feed temperature or temperature difference across the membrane which controls the membrane flux [7,17–19]. However, an increase in temperature reduces the energy barrier for nucleation, alters the solubility curve of the solution and increases the supersaturation rate (by increasing flux). The revised mass and heat transfer characteristics also modify the extent of concentration polarisation within the interfacial boundary layer subsequently adjusting the kinetics of nucleation and crystal growth. These interdependencies make it difficult to independently characterise the specific implications of using temperature or temperature difference to initiate nucleation and growth in different regions of the MSZW. In principle, for a fixed flux, an increase in membrane area can adjust supersaturation rate while sustaining comparable boundary layer characteristics. According to the theoretical approach of Nývlt (1968), the supersaturation rate is also dependent upon initial solute mass (magma density) and volume. The magma density can alter the vapour pressure but will also modify the solute concentration within the interfacial boundary layer, whereas the solution volume can be used to adjust supersaturation rate without implication to the boundary layer. In principle, solution volume can therefore be used to transition across the MSZW, and independently characterise how each of these factors individually inform on the kinetics of nucleation and crystal growth.

While the MSZW is recognised to play a critical role in controlling primary nucleation, characterisation of the MSZW has been rarely reported in the membrane crystallisation literature, requiring the accurate determination of induction time [9,20]. To date, induction time has been primarily inferred from the rapid decline in membrane flux [12,17]. However, it is widely recognised that these two phenomena are mechanistically distinct [12]. Jiang et al. [13] provided one of very few studies to relate the maximum MSZW boundary (ΔC_{max}) to the supersaturation through control of feed temperature and temperature difference (ΔT) [13]. In their study, nucleation kinetic parameters were ascertained but they were not correlated to the primary nucleation mechanism, which determines the probability for scaling, or to crystal growth phenomena, which are also strongly informed by where within the MSZW that nucleation occurs. In this study, we intend to independently characterise each of the critical parameters that determine the supersaturation rate as a basis on which to inform control strategies for MDC that offer a deterministic approach to crystallisation. In-line turbidimetry is applied for the accurate determination of induction time as a method to systematically characterise the MSZW, thereby relating the physical environment to the kinetics of nucleation and crystal growth. Specific objectives are to: (i) characterise methods for modulating supersaturation rate in MDC by transforming data to describe primary nucleation kinetics across the MSZW; (ii) differentiate between regions in which homogeneous and heterogeneous nucleation (scaling) are likely to predominate; (iii) determine regions within the MSZW that foster specific crystal growth characteristics; and (iv) establish a framework that can collectively describe how nucleation and crystal growth can be facilitated through a broad set of kinetic trajectories.

2. Materials and methods

2.1. MDC experimental setup

Commercial polypropylene hollow fibre membranes (Accural 300/1200, 3 M, Wuppertal, Germany) with a porosity of 73 ± 2 %, pore size of 0.45 μm and wall thickness 300 μm, were used in this study (Table 1). The hollow fibre membranes were potted and sealed into end plates and mounted into an acrylic membrane housing with an internal diameter and length of 15 mm and 150 mm respectively. Two membrane modules were constructed with 7 and 37 hollow fibres comprising an effective membrane area of 59.4 cm^2 and 313.9 cm^2 respectively (Table 1) and operated in a direct contact membrane distillation configuration (Fig. 1). The feed solution (sodium chloride, 23.9 wt% and 25.9 wt%) was introduced into the shell-side and maintained at a temperature of 55 ± 1 °C using a heater and heat exchanger assembly (Tornado TM IS6, HUBER Ministat230; Radleys, Saffron Walden, UK). Deionised water was cooled down using a chiller (LT ECOCOOL 150, Grant Instruments, Shepreth, UK) and introduced counter current into the hollow fibre lumen side. Feed and permeate temperatures were measured with in-line thermocouples (El1034 Temperature Prop, LabJack Corporation, Lakewood, USA). Feed and permeate velocities were fixed at 0.06 m s^{-1} and laminar flow was reliably maintained (Reynold number < 2000) for each membrane module using a peristaltic pump (Masterflex L/S Digital Pump System, Cole Parmer, St. Neots, UK), where temperature difference across the membrane was maintained at 20 ± 2 °C and 10 ± 2 °C. The permeate flux was measured experimentally using a balance (±0.5 g accuracy, LBX model bench scale, Adam Equipment Co Ltd, Milton Keynes, UK). For each condition, experiments were conducted in triplicate, and the average was recorded. Example primary data are included within Appendix A, plotted as an average of the triplicated experiments.

2.2. Characterisation of nucleation, crystallisation and surface scaling

An in-line turbidity sensor was used which employs a backscatter technique to determine induction (InPro8200/S/Epoxy/120, Mettler Toledo, Manchester, UK), which comprises of a dual optic fibre construction to provide greater sensitivity for nucleation detection. Induction time is a measure of metastability and is defined by the difference in time between when the system achieved saturation and the saturation at which nucleation commenced, which was determined using turbidimetry (see Appendix A for primary data). The produced crystals were

Table 1
Membrane and module specification.

Property	Units	Value	Fibre no.	
			7	37
Internal diameter	(di, m)	0.0012		
Outer diameter	(do, m)	0.0018		
Wall thickness	(m)	0.0003		
d_i/d_o	–	0.67		
Pore size	(μm)	0.45		
Porosity	(%)	73 ± 2		
Contact angle[a]	(°)	131		
Fibre length	(m)	0.15		
Shell inner diameter	(m)	0.015		
Packing density	(%)		10.2	53.9
Membrane area	(cm^2)		59.4	313.9

[a] Measured using water [42].

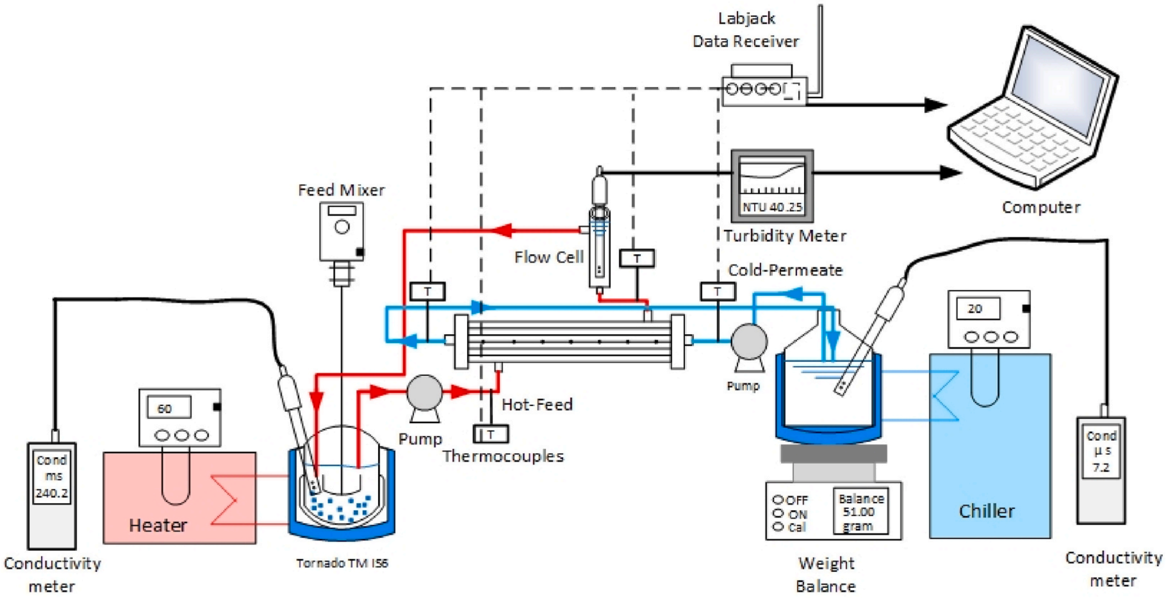

Fig. 1. Schematic diagram of the MDC setup.

collected by filtering feed solution through a 0.45 μm nylon filter (Whatman, Dorset, UK). The crystals were dried over a desiccant (Genlabs drying cabinets 200 L, Zoro, London, UK) for 48 h (temperature ~23 °C) before weighing with a high precision balance (range 0.02–62 g, error ±0.0001 g, Fisherbrand™, Loughborough, UK). Crystal size distributions were performed using optical microscopy (Lumenera Infinity 3-3 Camera with lens, 5/0.12 160/-) and images analysed using Image ProPremier software (v9.2, Media Cybernetics, Rockville, US). CSD was determined for each set of experimental conditions and comprised a minimum of 800 crystals to minimise the standard error of the distribution. The membrane module was collected after the experiment and dried over desiccant for 72 h, before being weighed. Membrane scaling/deposition was expressed as crystal weight per membrane area (g m^{-2}). All experiments were conducted in triplicate as a minimum, and the average reported.

2.3. Data analysis

The Permeate flux (N) (kg m^{-1} h^{-1}) was calculated as follows [21]:

$$N = \frac{m}{A \times \Delta t} \tag{1}$$

where m is the permeate mass (kg), A is membrane area (m^2), and Δt represents the time interval (h). The bulk feed solute concentration was estimated based on a permeate flux mass balance, while using direct monitoring of permeate conductivity to confirm the permeate solute concentration. In the membrane boundary layer, the film concentration C_{fm} deviates from that of the bulk feed solution, C_f, due to concentration polarisation (CPC), which was calculated based on the film mode [22]:

$$CPC = \frac{c_{fm}}{c_f} = exp\left(\frac{N}{\rho \times k_s}\right) \tag{2}$$

where C_{fm} and C_f (g NaCl. g^{-1} solution) are the membrane film concentration and bulk feed concentration respectively, ρ is solution density (kg m^{-3}) and k_s is the solute mass transfer coefficient (m s^{-1}) which can be evaluated from Chilton-Colburn analogy [23,24]:

$$\frac{Sh_f}{Sc_f^{0.33}} = \frac{Nu_f}{Pr_f^{0.33}} \tag{3}$$

where Sh_f is the Sherwood number, Sc is the Schmidt number, Nu_f is the Nusselt number and Pr_f is the Prandtl number of feed solution.

$$Sh_f = \frac{k_s D_h}{D_s} \tag{4}$$

$$Sc_f = \frac{\mu_f}{P_f D_s} \tag{5}$$

$$Nu = 1.86\left(Re Pr\, D_h/_L\right)^{0.33} \tag{6}$$

$$Re = \frac{d_h V \rho}{\mu} \tag{7}$$

$$Pr = \frac{C_p \mu}{k_s} \tag{8}$$

where Re is Reynold number (–), D_h is hydraulic diameter (m), D_s is solute diffusion coefficient (m^2 s^{-1}), μ is viscosity (Pa s^{-1}), L is the hollow fibre length (m), v is the feed velocity (m s^{-1}). All solution properties were obtained for the relevant temperature and concentration from Aspen Plus software using the Elec-NRTL thermodynamic model which is suitable for highly-concentrated electrolyte solutions [25]. The heat transfer in membrane distillation consists of the latent heat Q_v (W m^{-2}) from the vapour flux, and conductive heat through the membrane Q_c (W m^{-2}) [21]:

$$Q = Q_v + Q_c = \left(\frac{k_m}{\delta_m}\right)(T_{fm} - T_{pm}) + NH_{V,T} \tag{9}$$

$$H_{V,T} = 1.7535\ T + 2024.3 \tag{10}$$

where $H_{V,T}$ is vapour latent heat (KJ kg^{-1}), k_m is membrane thermal conductivity (W m^{-1} K^{-1}) and δ_m is the membrane thickness (m) [26]:

$$k_m = k_p(1 - \varepsilon) + k_g \varepsilon \tag{11}$$

where k_p (W m^{-1} K^{-1}), and k_g (W m^{-1} K^{-1}) are the polymer thermal conductivity and the air thermal conductivity respectively, while Ɛ is membrane porosity and T is the average temperature at the membrane surface (K) [26,27]:

$$T = \frac{T_{fm} + T_{pm}}{2} \tag{12}$$

T_{fm} and T_{pm} are the feed and permeate temperature at the membrane vicinity [17,21]:

$$T_{fm} = T_f - \left(T_f - T_p\right)\left[\frac{1/h_f \times d_i/d_o}{1/h_f \times d_i/d_o + 1/(h_m + h_v) + 1/h_p}\right] \tag{13}$$

$$T_{pm} = T_p - \left(T_f - T_p\right)\left[\frac{1/h_p}{1/h_f \times d_i/d_o + 1/(h_m + h_v) + 1/h_p}\right] \tag{14}$$

where T_f and T_p (k) are the bulk temperature in feed and permeate, d_i/d_o is inner/outer diameter ratio, $h_m = k_m/\delta_m$ (W m^{-2} K^{-1}) is membrane heat transfer coefficient, and h_v is the vapour heat transfer coefficient (W m^{-2} K^{-1}):

$$h_v = \frac{NH_{v,\left(T_{fm}+T_{pm}\right)/2}}{\left(T_{fm} - T_{pm}\right)} \tag{15}$$

where h_f (W m^{-2} K^{-1}) is feed heat transfer coefficient and h_p (W m^{-2} K^{-1}) is the permeate heat transfer coefficient:

$$h_{f,p} = Nu \times \frac{k_{f,p}}{d_{h_{f,p}}} \tag{16}$$

where k_f (W m^{-1} K^{-1}) is the thermal conductivity of feed and k_p (W m^{-1} K^{-1}) is the thermal conductivity of the permeate, d_{hf} and d_{hp} are the hydraulic diameter of feed and permeate flow channel and *Nu* is the Nusselt's number. Therefore, the temperature polarisation coefficient was calculated by iteration from the heat transfer relationship:

$$TPC = \frac{T_{fm} - T_{pm}}{T_f - T_p} \tag{17}$$

The nucleation mechanism was analysed based on classic nucleation theory where the change in critical free energy ΔG* can be expressed as follows [28]:

$$\Delta G^{*} = \frac{16\pi v_{\circ}^{2}\gamma^{3}}{3(k_B T)^{2}\, ln^{2}\, s} \tag{18}$$

where ΔG* is the critical nucleation barrier at a given supersaturation, k_B is the Boltzmann constant (1.38 × 10^{-23} J K^{-1}), T is the nucleation temperature (K), S is supersaturation (C/C*, unitless) and γ is interfacial energy (mJ m^{-2}). The molar volume (v_0, m^3) is:

$$v_0 = \frac{M}{\rho N_a} \tag{19}$$

v_o is the molar volume (m^3), ρ_{cry} is crystal density (kg m^{-3}), N_a is Avogadro's number (6.022 × 10^{23} molecules mol^{-1}). According to Arrhenius's approach, the nucleation rate J (No. m^{-3} s^{-1}) is given as follows [29]:

$$J = A\ \exp\left(-\frac{\Delta G*}{K\ T}\right) = A\ \exp\left(-\frac{16\pi v_{\circ}^{2}\gamma^{3}}{3(k_B T)^{3}\ ln^{2}\ s}\right) \tag{20}$$

The nucleation rate is related inversely to induction time which can be related to the extent of supersaturation (Zhou, 2017):

$$t_{ind} \propto \frac{1}{J} \tag{21}$$

$$\ln\, t_{ind} = \ln A + \left(\frac{16\pi v_{\circ}^{2}\gamma^{3}}{3(k_B T)^{3}\ ln^{2}\ s}\right) = \ln A + \left(\frac{B}{ln^{2}\ s}\right) \tag{22}$$

where A (m^{-3} s^{-1}) is the pre-exponential kinetic parameter, B is the thermodynamic parameter for nucleation [30]. Linearisation of the relationship between ln (t_{ind}) and 1/(ln^2S), yields lnA as the intercept and B as the gradient, enabling calculation of critically dependent crystallisation parameters, where the dominant nucleation mechanism (homogenous or heterogenous) can be evidenced from the gradient of the obtained slope.

The MSZW was analysed by adaption of the approach proposed by Nŷ; vlt (1968) [13], where the maximum MSZW limit identified at the membrane surface $\Delta C_{max.fm}$ (mg. g^{-1} solution) is assumed to be proportional to the concentrating rate R' (g 0.100 g solution. h^{-1});

$$\Delta C = \left(\frac{dC}{dT}\right)_T R' \tag{23}$$

$$R' = \left(\frac{dCo}{dt}\right)_t = \frac{F_P C_0}{m_0 - \int_0^t F_P d\tau} \tag{24}$$

where F_p is permeate flow rate (kg h^{-1}), m_o is feed solution mass (kg), C_o is the equilibrium concentration (g NaCl. g^{-1} solution). This provides for the normalisation of each factor (membrane area, flux, temperature difference, crystalliser volume, magma density) into a single term. By assuming that the supersaturation rate is equal to nucleation rate at induction, the relationship between nucleation rate (*J*) and the maximum MSZW limit at the membrane surface $\Delta C_{max.fm}$ was expressed by an empirical power-law relationship [13,14]:

$$J = k\left(\Delta C_{max,fm}\right)^{n} \tag{25}$$

where $\Delta C_{max,fm}$, (which is, c_{fm}-c*) is the maximum supersaturation within the membrane boundary layer. Therefore, the maximum supersaturation boundary at the membrane film $\Delta C_{max,fm}$ is proposed to be proportional to the concentrating rate R′, where both correspond to the nucleation rate:

$$J = k\left(\Delta C_{max,fm}\right)^{n} = \left(\frac{dc_0}{dt}\right)_t = \frac{F_P C_0}{m_0 - \int_0^t F_P d\tau} \tag{26}$$

Taking logarithms for both sides of eq. (23), the nucleation constant (k) and nucleation order can be determined from a linear fit between lnR' and ln $\Delta C_{max,fm}$:

$$\ln\left(\Delta C_{max,fm}\right) = \frac{1}{n}\ln\left(\frac{C_0}{k}\right) + \frac{1}{n}\ln\left(\frac{F_p}{m_0 - \int_0^t F_P d\tau}\right) \tag{27}$$

3. Result and discussion

3.1. *Characterising flux and induction time to transform into supersaturation rate*

The individual parameters that collectively determine the supersaturation rate in MDC were independently examined (membrane area, magma density, temperature difference). For each parameter, solution volume was used to transition across the MSZW. An increase in solution volume does not alter mass and heat transfer conditions across the membrane, enabling consistent boundary layer conditions when transitioning across the MSZW. Consequently, the water vapour flux established for each individual parameter was comparable across the solution volumes tested (Fig. 2). However, there were differences in the fluxes attained for each parameter (Table 2). When ΔT was decreased from 20 to 10 °C in the 37 HF module, flux reduced from 2.72 ± 0.19 to 1.0 ± 0.11 kg m^{-2} h^{-1}, due to the reduction in vapour pressure difference (from 5.10 to 3.02 kPa, Appendix B) which is the driving force for permeation [7]. This reduced temperature and concentration polarisation within the boundary layer. The flux attained for the 7 and 37 HF modules (ΔT 20 °C, 23.9 wt%) were similar at 3.20 ± 0.19 and 2.72 ± 0.19 kg m^{-2} h^{-1} respectively. The reduction in flux for the 37 HF module may have arisen from the preferential flow patterns within the larger fibre bundle which are noted to lower superficial velocity [31]. This slightly reduced the CPC and TPC within the film due to the lower mass and heat transfer. Increasing magma density from 23.9 to 25.9 wt% reduced the flux from 2.72 ± 0.19 to 2.31 ± 0.12 kg m^{-2} h^{-1} due to modification of the vapour pressure. The reduction in flux compensated

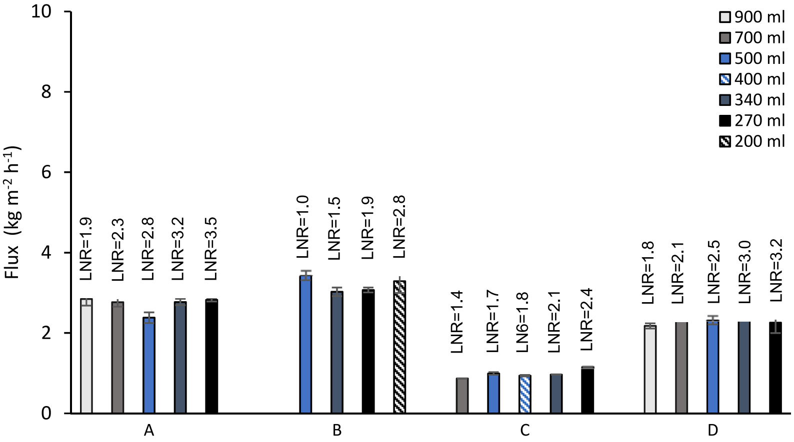

Fig. 2. Average permeation flux before induction for different primary supersaturation parameters: (A) 37HF, 23.92%wt, ΔT 20 ± 2 °C; (B) 7HF, 23.92%wt, ΔT 20 ± 2 °C; (C) 37HF, 23.92%wt, ΔT 10 ± 2 °C; (D): 37HF, 25.92%wt,ΔT = 20°±2C. Boundary conditions: T_{bulk}, 55 ± 1 °C; feed and permeate velocity, 0.06 m s^{-1}.

Table 2
Average concentration and temperature polarisation before induction for different supersaturation parameters.

Fibre no.	Bulk temperature (°C)	Temperature differences ΔT (°C)	Initial feed concentration (wt. %)	Concentration polarisation (CPC)	Temperature polarisation (TPC)
7HF	55 ± 1	20 ± 2	23.9	1.054 ± 0.01	0.55 ± 0.03
37HF	55 ± 1	20 ± 2	23.9	1.025 ± 0.004	0.59 ± 0.01
37HF	55 ± 1	10 ± 2	23.9	1.010 ± 0.001	0.69 ± 0.01
37HF	55 ± 1	20 ± 2	25.9	1.025 ± 0.01	0.60 ± 0.01

for the increased solute concentration leading to an equivalent CPC and TPC.

For each parameter, a steady-state period of flux was followed by a rapid decline in flux with every volume tested (Fig. 3). The steady-state period is defined by a slow and slight decrease in flux due to the reduction in vapour pressure which was in proportion to the progressive increase in feed concentration following permeation. The rapid decline in flux has traditionally been thought to signify the onset of nucleation [20]. An increase in feed volume increased the time before the rapid flux decline began. To illustrate, the time required to the onset of rapid flux decline reduced from 100 min at 900 ml to 46 min at 270 ml for the 37 HF membrane module (ΔT, 20 °C; magma density, 23.9%wt.). Reconstruction of the data based on supersaturation, revealed that the highest supersaturation was achieved for the smallest volume, which corresponded to the shortest filtration time. Turbidimetry provided a more accurate quantitation of the onset of nucleation (induction) by determining the time at which crystallisation began in the bulk solution (Fig. 4). The time between the solubility limit (c/c*, 1) and the obvious change in turbidity is defined as the induction period, and confirmed that primary nucleation occurred in each condition tested. Induction time for the 37HF module decreased from 33 min for 900 ml to 22 min for 270 ml, while the supersaturation at induction increased from 1.04 to 1.16 respectively. While of an equivalent initial concentration, a larger volume exposed to the same flux (and membrane area) will take longer to achieve an equivalent level of supersaturation, and it is this reduced rate which is instigated by the increase in volume, that aids kinetic moderation within this non-equilibrium condition in which different intermediate energetic states can be achieved based on the rate applied. Volume is therefore comparable to any other factor that may control the kinetic transition across the metastable zone width (e.g. ΔT), the difference being that ΔV can modify the metastable state without substantively altering mass and heat transfer processes within the boundary layer. The supersaturation levels determined through the flux curves were 1.05 and 1.17 respectively, which indicate a short lag between bulk crystallisation and the diminution of flux, which implies that this may primarily relate to the deposition of crystals formed previously through a homogeneous mechanism in the bulk solution. Importantly, the inverse relationship established between induction time and supersaturation is a characteristic response for kinetically controlled crystallisation [1,32,33]. Comparable analyses were also conducted for changes to membrane area, magma density and ΔT to distinguish the extent to which they influence primary nucleation through modification of supersaturation and induction time (primary data for all parameters within Appendix A).

3.2. *Supersaturation rate sets the position for nucleation within the metastable zone*

The extent of supersaturation achieved within the bulk solution and within the membrane boundary layer (film) at induction was determined across the MSZW following an increase in membrane area. For both membrane modules (37 and 7HF modules), the supersaturation achieved at induction within the boundary layer and bulk solution were demonstrated to increase when higher supersaturation rates (LnR’, g 100 g^{-1} solution h^{-1}) were instigated by a reduction in feed volume (Fig. 5). This response was observed for each parameter and is consistent with the kinetically derived model of Nývlt (Eq. (24)) which proposes higher supersaturation rates can be achieved for smaller crystalliser volumes [34–36]. For each membrane, the film concentration achieved at induction was consistently higher than the bulk concentration due to concentration and temperature polarisation. The ratio between bulk and film supersaturation levels achieved at induction were broadly consistent when the concentrating rate was increased, confirming that the boundary layer was not modified when using volume to regulate transition across the MSZW (Fig. 5a).

However, broader MSZW were achieved at induction when applying a higher area to volume ratio (A/V_o) (Fig. 5b). For an initial volume of 270 ml, magma densities of 28.9 and 31.3 wt% were determined for the 7 and 37HF membrane (A/V_o 21.9 and 116.2 m^2 m^{-3}) respectively. The broader MSZW is attributed to the higher concentrating rate achieved

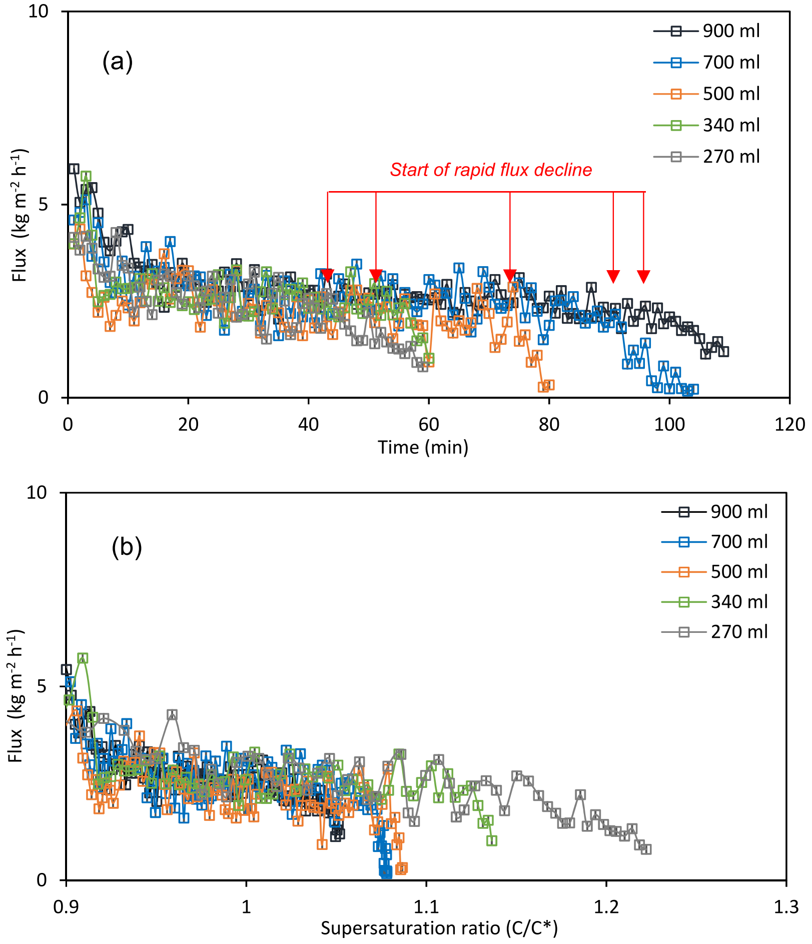

Fig. 3. Permeation flux for the 37 HF module across the solution volumes tested based on: (a) operating time; and (B) bulk supersaturation. Boundary conditions: T_{bulk},55 ± 1 °C; ΔT membrane, 20 ± 2 °C; feed and permeate velocity, 0.06 m s^{-1}; initial feed concentration 23.9 wt% NaCl. Data represents the average of permeation flux data from three replicated experiments undertaken at each volume.

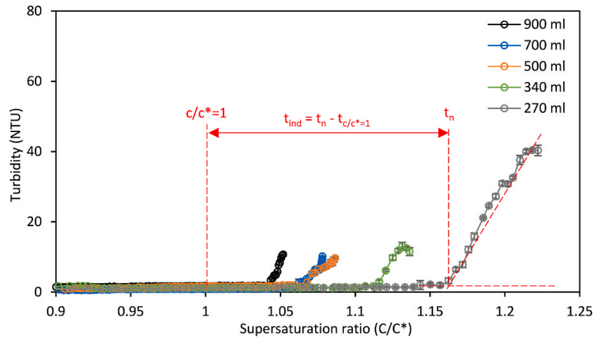

Fig. 4. *Turbidity profile for the 37 HF module operation. The supersaturation data reported is based on bulk conditions at different supersaturation rates across the solution volumes tested. Boundary conditions:* T_{bulk},*55 ± 1°C; ΔT membrane, 20 ± 2°C; feed and permeate velocity, 0.06 ms*$^{-1}$*; initial feed concentration 23.9 wt % NaCl.*

with 37HF [13,36], which is consistent with the characterisation approach of Sangwal [15] that assumes a linear correlation between concentrating rate and MSZW (Fig. 5c). This is evidenced through the explicit characterisation of the MSZW. For the 37 HF membrane, the maximum metastable limit ($\Delta C_{max,fm}$) increased from 2.99 mg_{solute} $g_{solution}^{-1}$ to 3.83 mg_{solute} $g_{solution}^{-1}$ when concentrating rate (LnR’) increased from 1.93 g 100 g^{-1} solution h^{-1} to 3.53 g 100 g^{-1} solution h^{-1}. Widening of the MSZW increases the driving force for nucleation by reducing the critical free energy barrier for nucleation. Elevated supersaturation develops within a kinetically controlled region (determined by the concentrating rate) of the MSZW that is seeking to establish the nearest metastable form (kinetically controlled), becoming less dependent on a heterogeneous substrate to initiate nucleation as ΔC_{fm} proceeds toward the outer metastable limit [16,37]. Importantly, both membranes exhibited comparable gradients for each slope (Fig. 5c), which describes the apparent nucleation order (Table 3), from which it can be inferred that the mechanism for formation and growth of stable nuclei is analogous regardless of the membrane area used. This implies nucleation to be deterministic at this scale and provides evidence of the continuity in kinetics that may be achieved in the scale-up of membrane crystallisation systems.

The concentrating rate decreased when ΔT was reduced from 20 ± 2 to 10 ± 2 °C due to the decline in vapour pressure gradient which lowered the driving force for permeation (N from 2.7 to 0.9 kg m^{-2} h^{-1}) (Fig. 6). This mitigated temperature and concentration polarisation in the film which adjusted the solubility curve and metastable limit. Consequently, a maximum metastable limit ($LnC_{fm,max}$) of 3.14 mg g^{-1} was achieved at ΔT 10 °C (270 ml) compared to 3.83 mg g^{-1} for ΔT 20 °C (270 ml) due to the reduction in supersaturation rate. The increase in temperature difference reduced the nucleation order, which indicates easier formation of stable nuclei [14]. This is because at a higher concentrating rate (higher ΔT), more intense intermolecular collisions are induced by the elevated localised concentration gradient within the

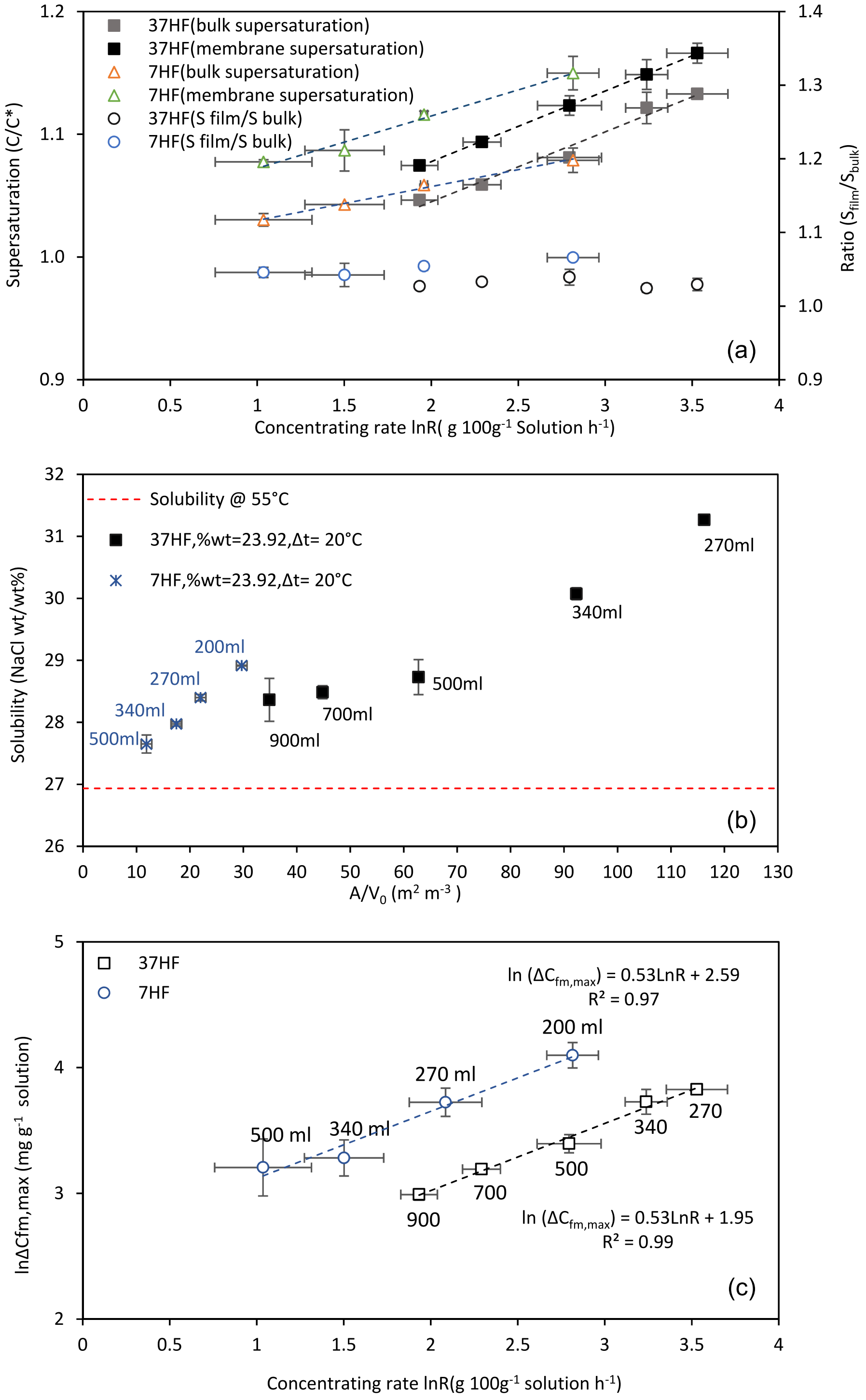

Fig. 5. (A) Bulk and membrane film supersaturation at induction based on concentrating rate (ln R′) adjusted by membrane area; (b) Metastable region characterised following the increase in area to volume ratio (A/V_o); (c) dependence of $\Delta c_{fm,max}$ in the film on concentrating rate (ln R′) according to Eq. (24). Boundary conditions: T_{bulk},55 ± 1 °C; ΔT20 ± 2 °C; feed and permeate velocity, 0.06 m s^{-1}; initial feed concentration 23.9 wt% NaCl.

boundary layer where the high solute concentration can rapidly overcome the free energy barrier for nucleation. The driving force for nucleation (supersaturation) within the boundary layer is further exacerbated by the reduced TPC which lowers the solubility limit to increase the metastable zone width. Increasing magma density from 23.9 to 25.9 wt% narrowed the MSZW due to the decrease in permeation flux imposed by the lower water activity (Figs. 2 and 6). The reduced flux (Fig. 2) decreased the concentrating rate and therefore the supersaturation level that was reached within the crystallising solution at induction. While temperature and concentration polarisation were relatively comparable, the reduction in mass transfer imposed by the higher magma density modified nucleation kinetics. A narrower MSZW was observed following an increase in concentrating rate, for the more concentrated magma density. Despite the comparable concentration polarisation observed for each magma density, which indicates a similar *relative* concentration difference between the bulk and film, the higher magma density increased the *absolute* solute concentration within the boundary layer from the outset. The relatively strong solute-solvent

Table 3
Analysis of nucleation parameters (based on correlation of ln (tind) versus 1/ln2S according to classical nucleation theory.

Fibre no.	Bulk temperature (°C)	Temperature differences ΔT (°C)	Initial feed concentration (wt. %)	Nucleation Order (n)	Nucleation constant (k)	Initial volume (ml)	Nucleation	Intercept (K)	Slope (m)	S (C/C*)	R^2
37HF	55 ± 1	20 ± 2	23.9	1.88	0.16	270–500	Homogeneous	3.00	0.0027	1.12–1.17	0.98
						700–900	Heterogeneous	3.34	0.0008	1.07–1.09	1.00
37HF	55 ± 1	10 ± 2	23.9	0.91	4.13	270–340	Homogeneous	2.87	0.0013	1.06–1.09	0.99
						400–700	Heterogeneous	3.42	0.0001	1.03–1.05	1.00
37HF	55 ± 1	20 ± 2	25.9	2.83	0.02	270–500	Homogeneous	2.16	0.0035	1.07–1.10	0.91
						700–900	Heterogeneous	2.98	0.0008	1.05–1.06	1.00
7HF	55 ± 1	20 ± 2	23.9	1.87	0.05	200–270	Homogeneous	3.18	0.0153	1.16–1.23	1.00
						340–500	Heterogeneous	3.92	0.0004	1.08–1.09	0.93

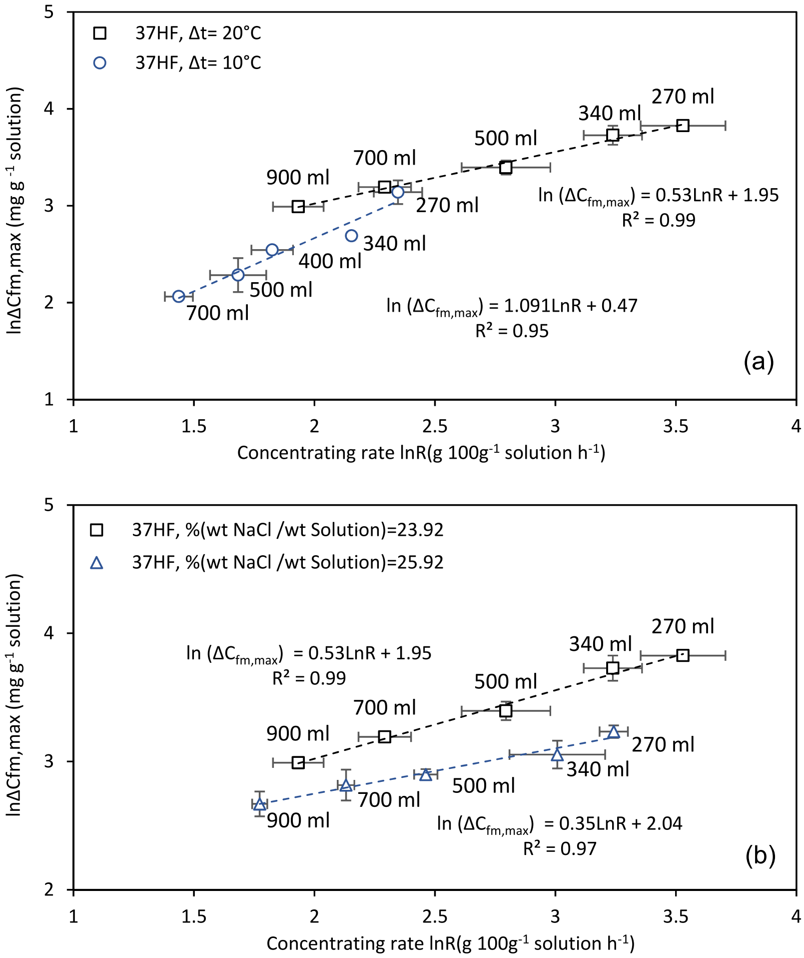

Fig. 6. *The dependence of $\Delta c_{max,fm}$ in the membrane film on concentrating rate (ln R′) for two sets of supersaturation rate parameters: (a) ΔT; and (b) different initial feed concentrations. Boundary conditions: T_{bulk}, 55 ± 1 °C; feed and permeate velocity, 0.06 ms^{-1}.*

interaction of NaCl coupled with the high solute concentration instigated from the outset, is known to reduce distance between solute ions sufficient to encourage solute aggregation that lowers the energy requirement for nucleation [15]. This was evidenced in this study by nucleation occurring at a lower concentrating rate and within a shorter induction time and is supported by the lower nucleation order attributed to the 25.92 % magma density (Fig. 6b).

3.3. Supersaturation rate determines extent of membrane scaling in MDC

Characterisation of the correlation between induction time (t_{ind}) and supersaturation ($\ln^2S$) evidences a transition between two slopes comprising distinct gradients, where the steeper slope formed at higher supersaturation is indicative of a homogeneous primary nucleation mechanism, while the shallow slope formed at low supersaturation implies that induction is regulated via a heterogenous primary nucleation mechanism [1,37] (Fig. 7). For each parameter that was characterised, a transition from heterogeneous to homogeneous primary nucleation was illustrated as supersaturation was increased through an increase in concentrating rate. The gradient of each distinct region of supersaturation can be used to infer the interfacial energy requirement to create a thermodynamically stable nucleus [32] (Table 3). While the reduction in ΔT from 20 to 10 °C reduced the supersaturation rate, comparable induction times were achieved within the lower region of the MSZW corresponding to where heterogeneous primary nucleation is most likely to proceed (Fig. 7, region marked A) [1,3,16,38]. This

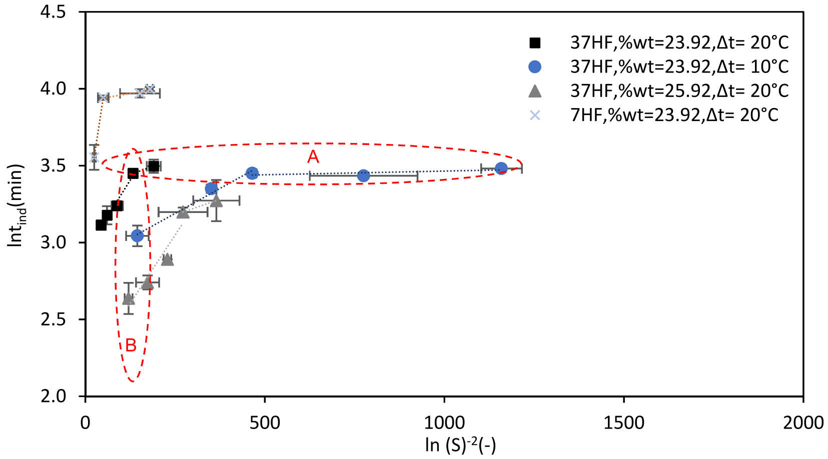

Fig. 7. *Characterisation of induction time (ln(tind)) and supersaturation (1/ln2S) at induction for different supersaturation parameters. Two distinct slopes are determined with the shallow slop infers a region dominated by primary heterogenous nucleation, while the steeper slope is characterised by a primary homogeneous nucleation mechanism at higher supersaturation. Boundary conditions: T_{bulk}, 55 ± 1°C; feed and permeate velocity, 0.06 m s^{-1}.*

implies that the energy barrier for nucleation was independent of the supersaturation level at induction and may be more dependent upon the role of the membrane in reducing the surface free energy required to pass the critical free energy barrier for. This is supported by the corresponding scaling rates, which were comparable within the heterogeneous region of the MSZW, despite differences in concentrating rate (Fig. 8). However, once transitioned into the homogeneous region of the MSZW, the gradient of the curve for ΔT 20 °C was around two times higher than for ΔT 10 °C, where the higher supersaturation levels achieved at shorter induction times foster considerably higher nucleation kinetics and mitigated scaling. To achieve the same supersaturation at induction ($\ln S^{-2}$, ~173), each parameter required a different induction

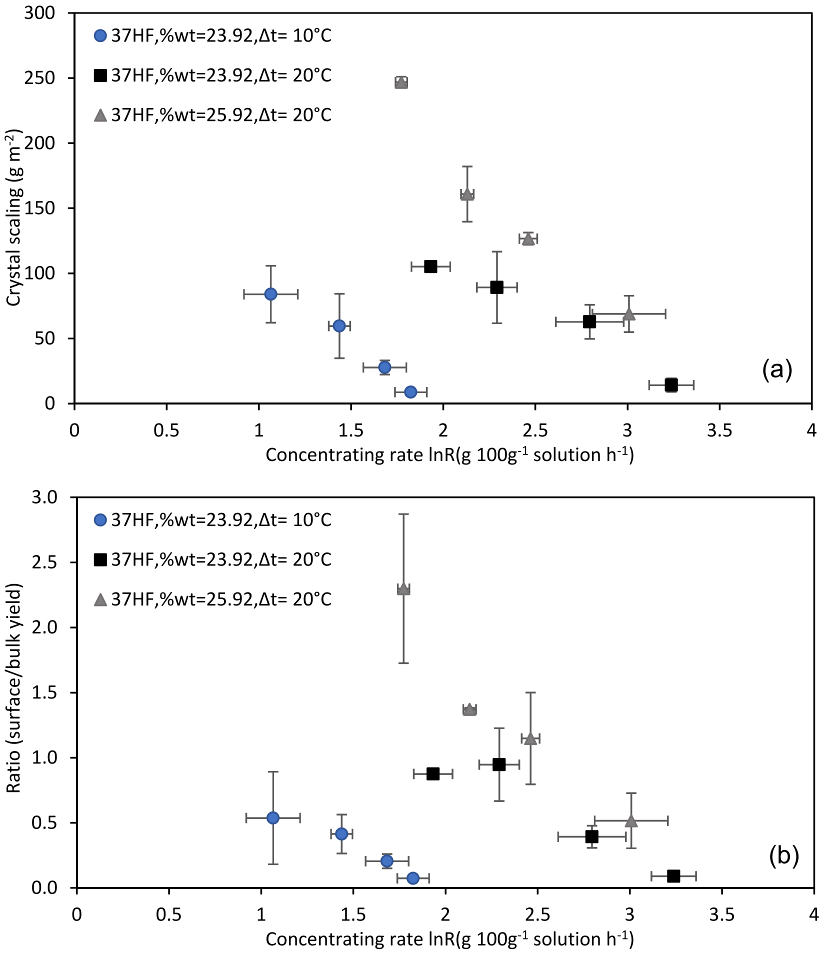

Fig. 8. *Extent of membrane scaling: (a) 37 HF module using different supersaturation parameters; and (b) comparison of crystal mass recovered from the bulk solution and from the membrane surface when using different supersaturation parameters. Boundary conditions: T_{bulk}, 55 ± 1°C; feed and permeate velocity, 0.06 ms^{-1}.*

time that was dependent on the concentrating rate applied (Fig. 7, region marked B). For higher concentrating rates, induction was determined within the homogeneous region of the MSZW and the membrane was characterised by negligible scaling, whereas longer induction times were synonymous with the heterogeneous region of the MSZW where substantive scaling occurred (Fig. 8). This increased dependency on an extrinsic heterogeneous substrate that can modify the critical free energy barrier at low supersaturation levels, requiring extended induction times, is compatible with classical nucleation theory [9,10,37]. Importantly, for each of the parameters outlined that regulate supersaturation, an increase in concentrating rate is evidenced to reduce the absolute scaling rate, despite a higher crystal yield (by mass) being produced within an elevated region of supersaturation (Fig. 8b). This provides corroborative data to suggest that the scaling mitigation observed was due to the suppression of scaling formed through an adhesive growth mechanism (heterogeneous nucleation) rather than a reduction in deposition by crystals formed in bulk solution following formation via homogeneous nucleation.

3.4. *Crystal growth is defined by the metastable zone width and supersaturation rate*

The kinetics of crystal growth inform the size and variance of the final product and are dependent upon where within the MSZW primary nucleation occurs [1,39]. Each of the parameters studied enable kinetic adjustment by uniquely modifying supersaturation at induction, the supersaturation rate and induction time to different extents. Crystal size distributions were therefore compared to determine how each parameter independently sets conditions for growth and were benchmarked using a fixed crystalliser volume (270 ml), which primarily corresponded to conditions that indicate favouring a homogeneous primary nucleation mechanism (Fig. 9). An increase in ΔT from 10 to 20 °C raised supersaturation rate to achieve a broader MSZW width at induction but at a comparable induction time (Lnt_{ind} 3.04 and 3.11 min). Median crystal size (L_{50}) increased from 69 ± 2 to 98 ± 4 μm and broadened the crystal size distribution (0th and 100th percentiles represented by whiskers). According to classical nucleation theory, an elevated concentrating rate should instigate higher nucleation rates that tend to produce a greater number of smaller crystals [32,37,40]. The larger crystals observed in this study may arise from Ostwald ripening which is recognised to occur following the nucleation of higher solubility solutes. Ostwald ripening does not imply a lower nucleation rate but rather the dissolution of small crystals followed by the accumulation of this solute into larger particles to reach a more thermodynamically stable state due to differences in chemical potential that can occur following desaturation (use of supersaturation for nucleation and growth). This accords with earlier observations of NaCl crystallisation in MDC, where Ostwald ripening was proposed to be driven by differences in particle sizeA difference in particle size may be driven through the supersaturation gradient that exists between the bulk and boundary layer in MDC, which are thought to independently drive crystal growth and nucleation respectively. In this study, an increase in membrane area established a higher supersaturation rate, which enabled a comparable supersaturation to be achieved at induction ($\ln C_{fm,max}$ 3.72 and 3.83 mg g^{-1} for 7 and 37HF respectively) but within a shorter induction time. A more comparable mean crystal size was observed (L_{50} 90 ± 1 and 98 ± 4 μm for 7 and 37HF respectively), while the CSD for 7HF comprised a lower variance. The higher crystal size attained with 7HF compared to that achieved with 37HF at ΔT 10 °C may be accounted for by the greater MSZW that was established, suggesting growth mechanisms to also dominate at the lower supersaturation rate imposed by the 7HF membrane. By using volume to modulate supersaturation, mass and heat transfer processes within the boundary layer are sustained, and as such the bulk supersaturation increases in proportion to the supersaturation in the film (Fig. 6A). This is in contrast to modification of the MSZW by altering ΔT or Re, where the adjustment of mass and heat transfer processes in the boundary layer can increase the boundary layer MSZW independent of the bulk solution [25]. The crystal growth sustained in this study at higher supersaturation may therefore also arise from the raised supersaturation within the bulk solution, that can continue to accommodate growth. Increasing magma density from 23.9 to 25.9 wt% fostered nucleation at a shorter induction time and at a lower supersaturation level while adopting a similar supersaturation rate. This decreased L_{50} from 98 ± 4 to 72 ± 6 μm when magma density increased from 23.9 to 25.9 wt% respectively and narrowed the size distribution. The shorter induction time is attributed to the higher absolute solute concentration instigated from the outset with the elevated magma density which reduces distance between solute ions to require lower supersaturation to drive nucleation, but the lower supersaturation reduces the chemical potential available to drive growth. Importantly, crystal size and variance of the distribution are recognised to underpin

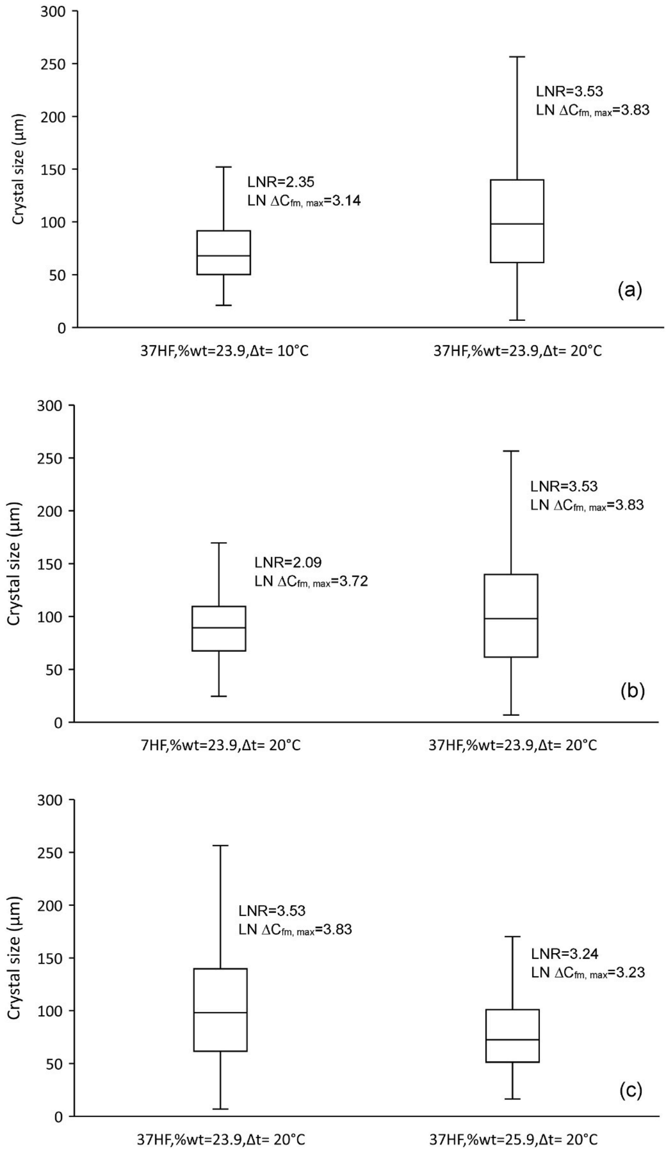

Fig. 9. *Crystal size distributions presented as box-whisker plots: (a) ΔT; (b) membrane area; and (c); different initial concentrations. Each parameter provides adjustment of one principal component of either supersaturation rate, supersaturation or induction time. Box represents upper and lower quartiles (25th and 75th percentiles), median size is indicted by the line within the box, and the whiskers represent the limited of the size distribution (0th and 100th percentiles). Boundary conditions: T_{bulk}, 55 ± 1 °C; feed and permeate velocity, 0.06 ms^{-1}; initial feed solution volume, 270 ml.*

crystal quality, and within this study several parameters are identified which independently govern the induction time, supersaturation and supersaturation rate in distinct ways that could be collectively applied to develop multiple kinetic trajectories for well-controlled crystal growth.

4. Conclusion

In this study, an analytical framework has been introduced to describe how multiple parameters collectively determine the supersaturation driving force in membrane distillation crystallisation which establishes the kinetics of nucleation and crystal growth. Many previous studies have sought to empirically relate water vapour flux to the kinetics of crystallisation. However, the direct measurement of induction time, complemented with membrane autopsy to characterise scaling, evidenced that for definitive characterisation, the supersaturation rate must be determined from MDC system characteristics (including flux) through a Nývlt-like approach as this can directly relate nucleation rate to the supersaturation instigated at induction providing a basis for the complete description of nucleation kinetics that offers a normalised approach enabling interstudy comparison.

Crystalliser volume enabled discrimination of how each parameter adjusted the MSZW without incurring complex boundary layer modifications. For each parameter, an increased dependency on the membrane to support primary heterogeneous nucleation was observed at low supersaturation levels and extended induction times which is compatible with classical nucleation theory. In the current membrane distillation literature, an increase in supersaturation rate (and supersaturation) is provided by an increase in temperature or temperature difference where the increased vapour flux enhances polarisation and leads to advanced scaling. Herein, the use of membrane-to-volume ratio, complemented by wider parameters (including T and ΔT) can deliver high supersaturation rates while mitigating scaling, and so provides a critically important approach for nucleation and crystal growth control in MDC that has not been previously described. The difference in response between the two approaches is driven by the extent to which the boundary layer is modified. The discontinuity with classical nucleation theory exhibited when using T and dT exclusively to modify nucleation kinetics deserves further study.

The NaCl system is characterised by a low crystal-liquid interfacial energy, that must strongly rely on a heterogeneous substrate to initiate nucleation due to the low supersaturation levels that can be achieved. While this represents a thermodynamic penalty, this study illustrates how kinetically controlled nucleation can mitigate scaling and implies that scaling can be easily mitigated for less soluble aqueous salts that possess considerably higher interfacial energy (e.g $CaSO_4$ relevant for seawater brines) and are thus more likely to nucleate through a homogeneous rather than adhesive growth (or heterogeneous) mechanism. Each parameter evaluated offered a distinct method of crystal growth modification, where either supersaturation rate, supersaturation or induction time could be sustained while the other two factors were amended. In general, higher supersaturation rates led to larger crystal sizes with broader size distributions, being related to Ostwald ripening within an elevated region of supersaturation. However, by achieving a high level of supersaturation at a lower supersaturation rate, an equivalent crystal size could be achieved with a narrowed size distribution. Consequently, while these parameters were independently investigated, synergistic strategies can be created through coupling of these collective factors to facilitate well-controlled crystal growth in membrane crystallisation systems. Importantly, this is distinct from classical evaporative crystallisers used for brines, where heat and mass transfer zones are disconnected, therefore offering limited scope for crystal growth modification strategies. Reproducibility was exemplified by the comparable nucleation kinetic constants obtained when increasing membrane area which indicate that comparable crystallisation characteristics can be achieved following scale-up of membrane crystallisation, which is a critical limitation to existing crystalliser design.

Author statement

A. Ouda: Conceptualization; Data curation; Formal analysis; Investigation; Methodology; Roles/Writing - original draft;

Y. Bajón Fernández: Writing - review & editing.

E. McAdam: Conceptualization; Data curation; Formal analysis; Funding acquisition; Investigation; Methodology; Project administration; Supervision; Writing - review & editing.

Declaration of competing interest

The authors declare that they have no known competing financial interests or personal relationships that could have appeared to influence the work reported in this paper.

Data availability

Data will be made available through a link to an open repository following peer review

Acknowledgements

This research was financially supported by European Research Council Starting Grant, ‘Sustainable chemical alternatives for reuse in the circular economy’ (StG, SCARCE, 714080). The data underlying this paper can be accessed through the following https://doi.org/10.17862/cranfield.rd.23136704.

Appendix A. Primary data flux data

Primary data for flux, evaluated by time and solution supersaturation, together with each turbidity trend, is presented. Primary data is accessible through the listed DOI. This includes primary data for membrane area, temperature difference and magma density.

Appendix B. Vapour pressure calculation

The Vapour pressure difference between feed and permeate (kPa) is calculated according to the Antoine’s equation as follow [41]:

$$\Delta P = \mathrm{P}_f - \mathrm{P}_p$$

$$\mathrm{P}_{\mathrm{f,p}} = \mathrm{P}^0(1 - \mathrm{x})\left(1 - 0.5\mathrm{x} - 10\mathrm{x}^2\right)$$

where x is the mole fraction of feed and permeate (mole) and P^o is the vapour pressure of pure water (kPa) calculated as follow:

$$P^0 = \exp\left(23.238 + \frac{3841}{T-45}\right)$$

where T is the feed and permeate temperature.

Appendix C. The probability for heterogeneous nucleation

The thermodynamic preference for heterogeneous nucleation of crystallisation on the membrane surface can be assessed by comparison of the free energy requirement to that of the homogeneous alternative:

$$\frac{\Delta G_{het}}{\Delta G_{hom}} = 0.25(2 + cos\ \theta)(1 - cos\ \theta)^2 \left[1 - \varepsilon \frac{(1 + cos\ \theta)^2}{(1 - cos\ \theta)^2}\right]^3 \tag{C1}$$

where ΔG_{het} and ΔG_{hom} are the free energies of heterogeneous and homogeneous nucleation respectively, θ is the contact angle between liquid and membrane surface and ε is the fractional porosity of the membrane [10]. For an equivalent liquid-surface contact angle and porosity to that applied in the study, the $\Delta G_{het}/\Delta G_{hom} = 0.83$. However, it is important to recognise that the genesis of this expression is grounded in the surface free energy requirement for nucleation, and therefore neglects the role of the volume free energy (ΔG_v) which describes the supersaturation requirement to initiate nucleation, and can be kinetically controlled by the modification of the supersaturation rate, which was the primary focus of this study.

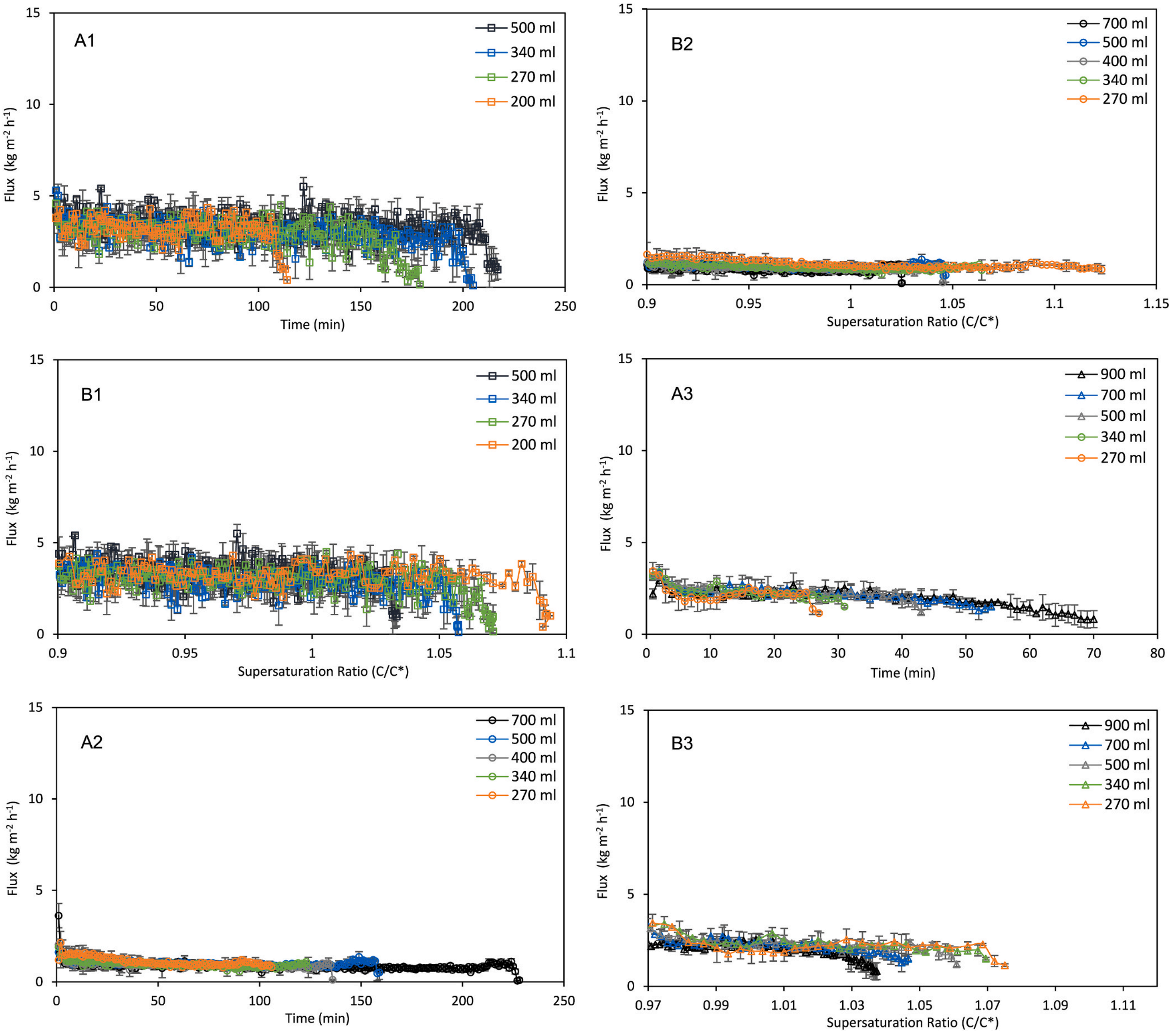

Fig. A1. *Permeation flux for different primary control variable: (A1,A2,A3); based on operating time; (B1,B2,B3); based on bulk supersaturation. Boundary conditions:* T_{bulk}, *55 ± 1 °C; Velocity of feed and permeate = 0.06* ms^{-1}.

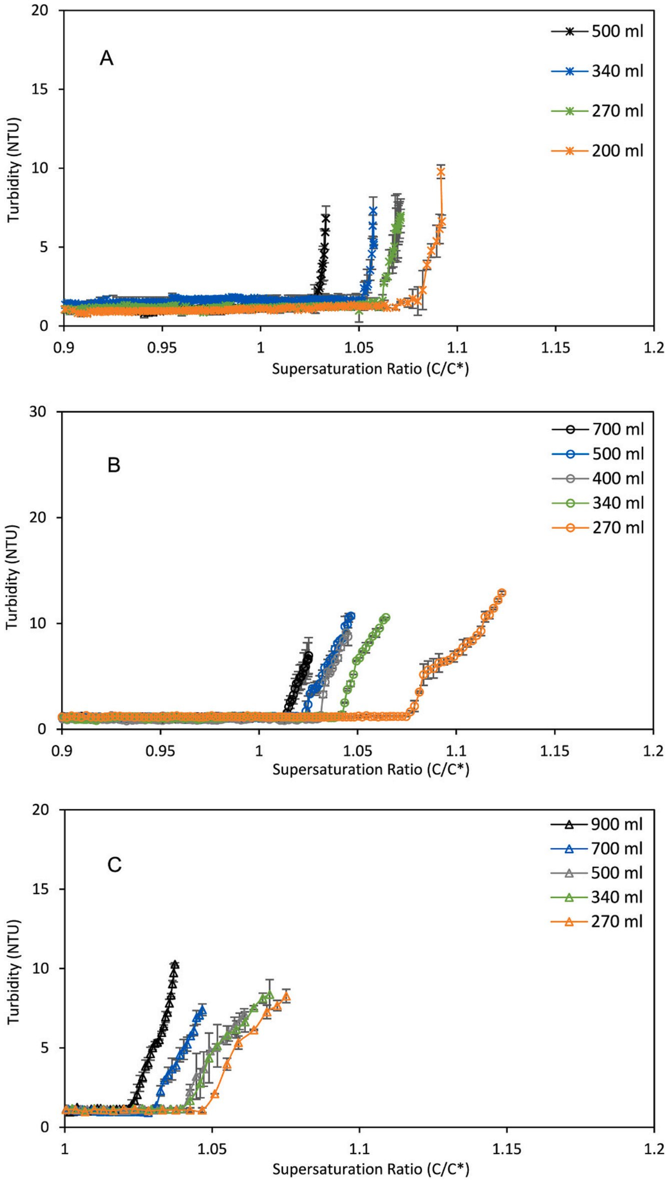

Fig. A2. Turbidity profile during MDC operation based on bulk supersaturation at different primary control variables. (A): 7HF, 23.9%wt., ΔT 20 °C; (B): 37HF, 23.9%wt, ΔT10 °C; (C): 37HF, 25.9%wt, ΔT 20 °C. Boundary conditions: T_{bulk} 55 ± 1 °C; feed and permeate velocity, 0.06 m s^{-1}.

References

[1] M. Lenka, D. Sarkar, Determination of metastable zone width, induction period and primary nucleation kinetics for cooling crystallization of L-asparaginenohydrate, J. Cryst. Growth 408 (2014) 85–90.

[2] F. Zou, W. Zhuang, J. Wu, J. Zhou, P.P. Yang, Q. Liu, Y. Chen, H. Ying, Determination of metastable zone widths and the primary nucleation and growth mechanisms for the crystallization of disodium guanosine 5′- monophosphate from a water-ethanol system, Ind. Eng. Chem. Res. 54 (2015) 137–145.

[3] E. Chabanon, D. Mangin, C. Charcosset, Membranes and crystallization processes: state of the art and prospects, J. Membr. Sci. 509 (2016) 57–67.

[4] J. Liu, Q. Wang, H. Shan, H. Guo, B. Li, Surface hydrophobicity based heat and mass transfer mechanism in membrane distillation, J. Membr. Sci. 580 (2019) 275–288.

[5] A. Caridi, G. Di Profio, R. Caliandro, A. Guagliardi, E. Curcio, E. Drioli, Selecting the desired solid form by membrane crystallizers: crystals or cocrystals, Cryst. Growth Des. 12 (9) (2012) 4349–4356.

[6] G. Chen, Y. Lu, W.B. Krantz, R. Wang, A.G. Fane, Optimization of operating conditions for a continuous membrane distillation crystallization process with zero salty water discharge, J. Membr. Sci. 450 (2014) 1–11.

[7] F. Edwie, T.S. Chung, Development of simultaneous membrane distillation-crystallization (SMDC) technology for treatment of saturated brine, Chem. Eng. Sci. 98 (2013) 160–172.

[8] E. Drioli, G. Di Profio, E. Curcio, Progress in membrane crystallization, Curr. Opin. Chem. Eng. 1 (2) (2012) 178–182.

[9] M.C. Sparenberg, S. Chergaoui, V. Sang Sefidi, P. Luis, Crystallization control via membrane distillation-crystallization: a review, Desalination 519 (2022), 115315.

[10] E. Curcio, G. Di Profio, E. Drioli, Probabilistic aspects of polymorph selection by heterogeneous nucleation on microporous hydrophobic membrane surfaces, J. Cryst. Growth 310 (24) (2008) 5364–5369.

[11] Y. Choi, G. Naidu, L.D. Nghiem, S. Lee, S. Vigneswaran, Membrane distillation crystallization for brine mining and zero liquid discharge: opportunities, challenges, and recent progress, Environ. Sci.: Water Res. Technol. 5 (7) (2019) 1202–1221.

[12] T. Horseman, Y. Yin, K.S. Christie, Z. Wang, T. Tong, S. Lin, Wetting, scaling, and fouling in membrane distillation: state-of-the-art insights on fundamental mechanisms and mitigation strategies, ACS ES&T Eng. 1 (1) (2021) 117–140.

[13] X. Jiang, X. Ruan, W. Xiao, D. Lu, G. He, A novel membrane distillation response technology for nucleation detection, metastable zone width measurement and analysis, Chem. Eng. Sci. 134 (2015) 671–680.

[14] G. Zeng, H. Li, S. Huang, X. Wang, J. Chen, Determination of metastable zone width and the primary nucleation kinetics of sodium sulfate, Theor. Found. Chem. Eng. 49 (6) (2015) 869–876.

[15] K. Sangwal, On the interpretation of metastable zone width in anti-solvent crystallization, Cryst. Res. Technol. 45 (9) (2010) 909–919.

[16] G. Di Profio, E. Curcio, E. Drioli, Supersaturation control and heterogeneous nucleation in membrane crystallizers: facts and perspectives, Ind. Eng. Chem. Res. 49 (23) (2010) 11878–11889.
[17] M.T. Chan, A.G. Fane, J.T. Matheickal, R. Sheikholeslami, Membrane distillation crystallization of concentrated salts - flux and crystal formation, J. Membr. Sci. 257 (1–2) (2005) 144–155.
[18] M. Hardikar, I. Marquez, T. Phakdon, A.E. Sáez, A. Achilli, Scale-up of membrane distillation systems using bench-scale data, Desalination 530 (2022).
[19] X. Zhang, R. Koirala, A. Date, V. Jegatheesan, Modelling and simulation of flux prediction and salinity variation in direct contact membrane distillation for seawater desalination and brine treatment, Desalination 540 (2022), 116021.
[20] X. Jiang, L. Tuo, D. Lu, B. Hou, W. Chen, G. He, Progress in membrane distillation crystallization: process models, crystallization control and innovative applications, Front. Chem. Sci. Eng. 11 (4) (2017) 647–662.
[21] X. Yang, R. Wang, L. Shi, A.G. Fane, M. Debowski, Performance improvement of PVDF hollow fiber-based membrane distillation process, J. Membr. Sci. 369 (1–2) (2011) 437–447.
[22] G. Chen, Y. Lu, X. Yang, R. Wang, A.G. Fane, Quantitative study on crystallization-induced scaling in high-concentration direct-contact membrane distillation, Ind. Eng. Chem. Res. 53 (40) (2014) 15656–15666.
[23] F. Edwie, T.S. Chung, Development of hollow fiber membranes for water and salt recovery from highly concentrated brine via direct contact membrane distillation and crystallization, J. Membr. Sci. 421-422 (2012) 111–123.
[24] M. Tomaszewska, M. Gryta, A.W. Morawski, Study on the concentration of acids by membrane distillation, J. Membr. Sci. 102 (C) (1995) 113–122.
[25] A. Jikazana, P. Campo, E.J. McAdam, Hydrodynamics (Reynolds number) determine scaling, nucleation and crystal growth in membrane distillation crystallisation, J. Membr. Sci. 685 (2023), 121909.
[26] A. Ali, J.H. Tsai, K.L. Tung, E. Drioli, F. Macedonio, Designing and optimization of continuous direct contact membrane distillation process, Desalination 426 (2018) 97–107.
[27] J. Phattaranawik, R. Jiraratananon, A.G. Fane, Heat transport and membrane distillation coefficients in direct contact membrane distillation, J. Membr. Sci. 212 (1–2) (2003) 177–193.
[28] S. Karthika, T.K. Radhakrishnan, P. Kalaichelvi, A review of classical and nonclassical nucleation theories, Cryst. Growth Des. 16 (11) (2016) 6663–6681.
[29] S. Wang, M. Feng, H. Du, J.J. Weigand, Y. Zhang, X. Wang, Determination of metastable zone width, induction time and primary nucleation kinetics for cooling crystallization of sodium orthovanadate from NaOH solution, J. Cryst. Growth 545 (2020), 125721.
[30] S. Karthika, T.K. Radhakrishnan, P. Kalaichelvi, Measurement of nucleation rate of ibuprofen in ionic liquid using induction time method, J. Cryst. Growth 521 (2019) 55–59.
[31] R. Thanedgunbaworn, R. Jiraratananon, M.H. Nguyen, Shell-side mass transfer of hollow fibre modules in osmotic distillation process, J. Membr. Sci. 290 (1–2) (2007) 105–113.
[32] S. Datta, D.J.W. Grant, Effect of supersaturation on the crystallization of phenylbutazone polymorphs, Cryst. Res. Technol. 40 (3) (2005) 233–242.
[33] G. Du, Z. Sun, Y. Xian, H. Jing, H. Chen, D. Yin, The nucleation kinetics of ammonium metavanadate precipitated by ammonium chloride, J. Cryst. Growth 441 (2016) 117–123.
[34] K. Sangwal, A novel self-consistent Nývlt-like equation for metastable zone width determined by the polythermal method, Cryst. Res. Technol. 44 (3) (2009) 231–247.
[35] D. Kashchiev, Note: on the critical supersaturation for nucleation, J. Chem. Phys. 134 (19) (2011), 196102.
[36] E. Mielniczek-Brzóska, Effect of sample volume on the metastable zone width of potassium nitrate aqueous solutions, J. Cryst. Growth 401 (2014) 271–274.
[37] G. Di Profio, S. Tucci, E. Curcio, E. Drioli, Controlling polymorphism with membrane-based crystallizers: application to form i and II of paracetamol, Chem. Mater. 19 (10) (2007) 2386–2388.
[38] J. Rolf, T. Cao, X. Huang, C. Boo, Q. Li, M. Elimelech, Inorganic scaling in membrane desalination: models, mechanisms, and characterization methods, Environ. Sci. Technol. 56 (12) (2022) 7484–7511.
[39] N. Kubota, A new interpretation of metastable zone widths measured for unseeded solutions, J. Cryst. Growth 310 (3) (2008) 629–634.
[40] J. Hou, S. Wu, R. Li, W. Dong, J. Gong, The induction time, interfacial energy and growth mechanism of maltitol in batch cooling crystallization, Cryst. Res. Technol. 47 (8) (2012) 888–895.
[41] A. Ali, C.A. Quist-Jensen, F. Macedonio, E. Drioli, Application of membrane crystallization for minerals' recovery from produced water, Membranes 5 (4) (2015) 772–792.
[42] C.J. Davey, M. Hermassi, E. Allard, M. Amine, N. Sweet, T.S. Gaite, A. McLeod, E. J. McAdam, Integrating crystallisation into transmembrane chemical absorption: process intensification for ammonia separation from anaerobic digestate, J. Membr. Sci. 611 (2020), 118236.